JOURNAL OF MAGNETIC RESONANCE **125,** 72–83 (1997)
ARTICLE NO. MN961073

# Simulation of $B_1$ Field Distribution and Intrinsic Signal-to-Noise in Cardiac MRI as a Function of Static Magnetic Field

R. W. SINGERMAN,* T. J. DENISON, H. WEN, AND R. S. BALABAN

*Laboratory of Cardiac Energetics, National Heart Lung and Blood Institute, National Institutes of Health, Bethesda, Maryland 20892-1061*

Received August 14, 1996; revised November 14, 1996

**Two issues that pertain to the optimal static magnetic field for cardiac MRI were addressed: intrinsic signal-to-noise ratio (ISNR) and radiofrequency power deposition. From 1.5 to 9.5 T, proton Larmor frequencies of 63 to 400 MHz, numerical simulations were performed of the RF fields from a surface coil and a body coil loaded by a heterogeneous, three-dimensional, symmetric model of the human chest. The RF field distribution, the power required to produce the RF field, and the ISNR at the center of the heart were computed. The model was validated by comparison with experimental data up to 4 T. The RF field distortion was quantified and found to increase linearly up to 6 T due mostly to dielectric resonance modes. Body coil simulations beyond 6 T showed the onset of higher-order modes at the center of the heart. A range of expected RF power requirements was constructed as a function of field up to 9.5 T for surface coils and up to 6.8 T for body coils. Over this range of static field, ISNR for a constant coil geometry was bracketed by an upper limit that was slightly greater than linear with field and a lower limit that was slightly less than linear with field. The RF power and ISNR showed a strong dependence on chest thickness at 1.5 and 4.0 T. Additionally, independent of chest thickness, the model predicts a lower limit of a factor of 5 increase in RF power as the static field is increased from 1.5 to 4 T. Implications for imaging with other nuclei are discussed. Methods for checking the self-consistency of electrodynamic simulations are presented.** 

## INTRODUCTION

Modeling the radiofrequency fields imposed on the body during MRI and computing the resulting RF losses and signal-to-noise ratios (SNR) have been areas of active research. Models have been used for estimating local RF power deposition, understanding image artifacts, designing RF coils, and predicting the utility of imaging at higher than existing static magnetic field strengths. Power depositions and SNR were initially computed for homogeneous body models in uniform applied RF fields (*1–5*). The mechanism for how transmitting and receiving in quadrature minimizes $B_1$ asymmetry artifacts and reduces RF power requirements has also been addressed. Model data on the effects of size and electrical parameters are also available and directly compared with experimental phantom data (*6*). Models introducing increasing levels of complexity, such as skin depth, dielectric effects, and surface charges, have been considered (*7, 8*). The RF field (up to 400 MHz) for a surface coil above a conducting dielectric sphere has been determined analytically (*9*). In contrast to homogeneous body models, more physiological heterogeneous body models have been proposed (*10*) and studied using finite element methods (*11*). Simulations have been performed on two-dimensional chest models (*12, 13*).

The intrinsic signal-to-noise ratio (ISNR), which is independent of relaxation properties, imaging artifacts, or instrument characteristics, has been proposed (*14*) as an objective method of field strength comparison for MRI. Additionally, other imaging parameters that influence the choice of magnetic field strength, such as relaxation times and chemical shifts, have been discussed (*15*).

In this study we build on previous work by performing numerical simulations of the RF fields in axially symmetric, heterogeneous, three-dimensional models which were scaled to be appropriate for cardiac MRI. This was done to gain insight into the static field dependence of the ISNR, $B_1$ distribution, and required power in cardiac MRI. Simulations were conducted between 1.5 and 9.5 T (proton Larmor frequencies of 63 and 400 MHz).

## MATERIALS AND METHODS

*Chest model.* The chest model was based on the transverse cross section of the male chest shown in Fig. 1 (NIH Visible Human Project, NIH home page on the World Wide Web). The outer chest layer is fat. The next layer is muscle. We note a variety of interface shapes between body layers. In particular, some interfaces are diffuse while others are quite sharp. For example, sharp edges exist between fat and muscle and between muscle and bone. For the purposes of this model, we did not focus on specific characteristics. Instead, we formulated a model that would capture general

* This research was performed while the author held a National Research Council Research Associateship.



1090-7807/97 $25.00

**FIG. 1.** Cross section of the NIH Visible Human Male Chest.

features. Hence, we chose a model with symmetrical corners that have the approximate curvature of the corner between the back and sides of the male chest. The four-layer cylindrically symmetric chest model consisted of a spherical heart inside a cylindrical can (representing the lungs) with a layer of fat and muscle surrounding the can. An annular surface coil used in this simulation is located above the can. Figure 2A shows an axially symmetric cross section of the surface coil on the chest model. The axis of symmetry is shown as a dashed rod through the center of the model. Simulations were performed with a surface coil or a body coil. For all simulations, the heart diameter is 12 cm, and the inner chest cavity dimensions are 21 cm from top to bottom and 27 cm across. In studies where the model size was changed, the fat thicknesses ranged from 0.5 to 2.0 cm, and the muscle thicknesses ranged from 1.0 to 3.0 cm.

*Body electrical parameters.* The RF field and RF power calculations depend strongly on the values of tissue electrical parameters such as dielectric constants and conductivities. The literature values (*16–18*) used for muscle and fat are given in Table 1. Blood and muscle have similar dielectric constants and electrical conductivities; hence the heart is modeled as muscle. We note that if the literature value of $\epsilon$ or $\sigma$ changed by less than 8% as a function of frequency, we held the value as fixed in the simulation. This choice was motivated by the roughly 5% error bars on the data points in the literature and interpolating between the data points (*16, 17*). This explains the use of ''constant'' $\sigma$ for muscle and ''constant'' $\epsilon$ and $\sigma$ for fat over the frequency range of the simulations. The physical source and interpretation of the behavior of $\epsilon$ and $\sigma$ in the frequency range of interest are briefly reviewed under Discussion.

As for lungs, simulations are first performed in which the lung space is modeled as an air-filled region. We refer to this as the four-layer model. In later sections, beginning with ''Estimating required power range for surface coil,'' calculations are also performed in which the lung space is modeled as a blood-filled region. We refer to this as the two-layer model. These two extremes for lung define lower and upper limits for required RF powers in our model. This bracketing of RF powers is discussed in more detail below.

*Coils.* For the surface coil simulations, a current sheet 1 cm wide and 25 cm in outer diameter is located 1 cm above the top of the model (see Fig. 2A). A body coil was used to create an approximately spatially uniform RF field. Figure 2B shows an axially symmetric cross section of the body model in the body coil. The body coil, a compensated solenoid, has a uniform current density, but the thickness of the end sections is twice the thickness of the middle. In the DC current limit, this current distribution creates a magnetic field that is uniform to sixth order (*19*). At 171 MHz, the unloaded compensated solenoid still produces a $B_1$ field that is homogeneous to a few percent across the dimensions of the body model that will be put into this field. We note that

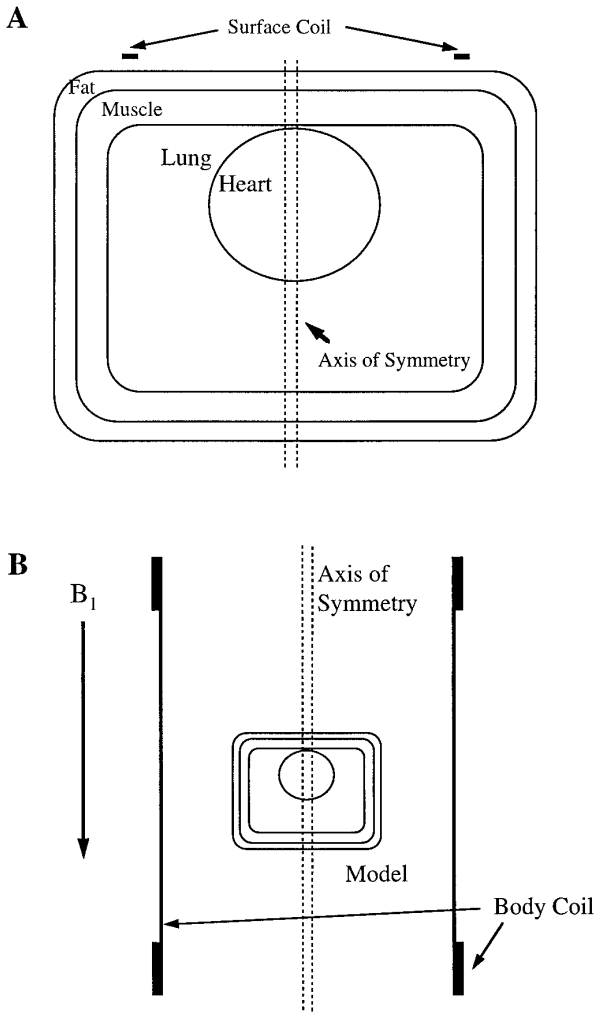


**FIG. 2.** Cross section of the four-layer, cylindrically symmetric, simulation chest model. The body and the coils share the same axis of symmetry. (A) Cross section of the circular surface coil (an annulus) on top of the chest. The surface coil is 1 cm wide and 25 cm in outer diameter. Fat thickness is 1.5 cm. Muscle thickness is 2.5 cm. Heart diameter is 12 cm. (B) Cross section of the body model in the body coil, a compensated solenoid.

the axis of the solenoid is coincident with the symmetry axis of the body model. Hence, the $B_1$ direction is also along the axis of symmetry. We do this, as opposed to employing a birdcage coil, in order to maintain the axial symmetry of the body model and coil system. This issue will be elaborated on further under Discussion.

In the simulations, one coil was simulated at a time (e.g., when the body coil was simulated, the surface coil was removed). Eddy current effects in the coils were not included. Thin coils were used to avoid penetration depth problems in the coils themselves. Finally, phase changes around the coil are not implemented. In experiments (*20*), such phase changes are minimized by designing surface coils with distributed capacitance.

*Boundary conditions.* For boundary conditions, the body and coil system is surrounded by a shield in the shape of a cylindrical can with its axis of symmetry coincident with the body and coil system. The shield is employed for computational purposes. Imposing a zero vector potential, and thus zero electric field for a cylindrically symmetric problem, at the shield is more efficient than boundary conditions that have fields become small far from the coils. However, the shield is far enough from the coil so that its perturbation on the field near the body is less than 1% of the shield free field calculation. For the surface coil simulation, the top of the shield is 55 cm above the center of the heart. The bottom of the shield is 55 cm below the center of the heart. The radius of the shield is 100 cm. For the solenoid (body coil) simulations, the shield is three solenoid radii above the top of the solenoid and three solenoid radii below the bottom of the solenoid and has a radial dimension that is three solenoid radii out from the solenoid. In terms of distances, this corresponds to the shield being 115 cm above the center of the heart, 115 cm below the center of the heart, and 90 cm radially out from the center of the heart.

*Computational resources.* The finite element mesh consisted of 10,000 to 20,000 triangles. Calculations were performed with Ansoft Corporation's 2 Dimensional Maxwell Simulator software, in axial symmetric mode, running on a Sun 1000 server with 256 Mbytes of RAM and a Sparc 20 coprocessor.

*Self-consistency checks in calculations.* In simulation studies, one must check limiting cases of calculations to check the software. The first simple check is to see if the simulation for an unloaded coil at low frequency approximately yields the correct field value at the center of the coil. If the annulus width is small compared to the inner radius of the annulus, then the field at the center of the circular annulus should be close to the field at the center of a circular current loop of the same radius, which can be computed exactly. The second check can be done by checking the simulated field value just above the annulus. At this point,

**TABLE 1**
**Dielectric Constants, $\epsilon$, and Conductivities, $\sigma$, Used for Simulations**

| Field (T) | $\epsilon_{muscle}$ | $\sigma_{muscle}$ (mmho/cm) | $\epsilon_{fat}$ | $\sigma_{fat}$ (mmho/cm) |
|---|---|---|---|---|
| 1.5 | 80 | 8.6 | 18 | 2.1 |
| 2.0 | 72 | 8.6 | 18 | 2.1 |
| 3.0 | 60 | 8.6 | 18 | 2.1 |
| 4.0 | 54 | 8.6 | 18 | 2.1 |
| 5.0 | 54 | 8.6 | 18 | 2.1 |
| 6.0 | 54 | 8.6 | 18 | 2.1 |
| 9.5 | 50 | 8.6 | 18 | 2.1 |

*Note.* Values are from *in vivo* dog measurements.

the annulus looks like an infinite current sheet. The field above the current sheet can also be computed exactly (*23*).

As a check on the loaded coil calculations, we can compare the power required to drive the coil with the power dissipated in the body. The power to drive the coil should equal the power radiated into space plus the power dissipated in the body. For negligible radiative losses, the power to drive the coil should equal the power dissipated in the body. In earlier studies of a surface coil above a conducting dielectric sphere (*9*), radiative losses were less than 5% of the total power dissipation for frequencies below 200 MHz. The power, $P_{\text{coil}}$, to drive an annular coil of inner radius $\rho_1$ and outer radius $\rho_2$ can be computed by evaluating the integral of $\mathbf{J}\cdot\mathbf{E}$ over the coil and time averaging over a cycle. In the time domain,

$$\int \mathbf{J}\cdot\mathbf{E}\,dV = \frac{I}{D}\int_{\rho_1}^{\rho_2}\oint_{C_\rho}\mathbf{E}\cdot d\mathbf{l}\,d\rho \qquad [1]$$

$$= -\frac{I}{D}\int_{\rho_1}^{\rho_2}\frac{1}{c}\frac{d\Phi(\rho)}{dt}\,d\rho, \qquad [2]$$

where $D = \rho_2 - \rho_1$, $I$ is the total current in the annulus, $C_\rho$ is a closed circular path of radius $\rho$, $d\Phi(\rho)/dt$ is the time derivative of the magnetic flux through $C_\rho$, and $c$ is the speed of light. We note that the simplification in Eq. [1] is possible because the current density was made uniform across the annular width, $D$, in the simulations. In the frequency domain, the equations become

$$P_{\text{coil}} = \frac{1}{2}\,\text{Re}\left[\int \mathbf{J}\cdot\mathbf{E}^*\,dV\right] \qquad [3]$$

$$= \frac{1}{2}\frac{I}{D}\int_{\rho_1}^{\rho_2}\frac{\omega}{c}\,\Phi_{\text{Im}}(\rho)\,d\rho \qquad [4]$$

$$\equiv \frac{1}{2}\frac{I\omega}{c}\,\langle\Phi_{\text{Im}}\rangle, \qquad [5]$$

where $\Phi_{\text{Im}}(\rho)$ is the imaginary part of the magnetic flux through $C_\rho$, and $\langle\Phi_{\text{Im}}\rangle$ is the spatial average of $\Phi_{\text{Im}}(\rho)$ over the width of the annulus.

In practice, we computed $\langle\Phi_{\text{Im}}\rangle$ by computing $\Phi_{\text{Im}}$ just above the annulus at eight equally spaced radii from the inner to the outer radius. At 171 MHz, $P_{\text{coil}}$ agreed with the power dissipated in the body, $P_{\text{body}}$, to within 1%.

## RESULTS

For the surface coil and body coil simulations, $B_1$, the circularly polarized transverse component of the RF field, was computed from $\mathbf{B}_1^{\text{total}}(\mathbf{r})$, the full RF field in the frequency domain:

$$B_1 \equiv \frac{\|\mathbf{B}_1^{\text{total}}(\mathbf{r})\cdot(\hat{\mathbf{x}} - \mathbf{i}\hat{\mathbf{y}})\|}{\sqrt{2}}. \qquad [6]$$

The power, $P_{90^\circ}$, required to produce a 1 ms, 90°, proton flip at the center of the heart was determined to normalize the field plots as well as to determine the ISNR. The $P_{90^\circ}$ is calculated using the equation

$$P_{\text{body}} = \tfrac{1}{2}\text{Re}\left[\int \sigma\mathbf{E}\cdot\mathbf{E}^*\,dV\right] \qquad [7]$$

and normalization:

$$P_{90^\circ} = \frac{P_{\text{body}}}{B_1^2/(B_1^{90^\circ})^2}. \qquad [8]$$

$\mathbf{E}$ is the electric field and $\sigma$ is the conductivity of the region. $P_{\text{body}}$ is the power dissipated in the body to produce $B_1$, $B_1^{90^\circ}$ is the circularly polarized magnetic field required for a 1 ms 90°, proton flip at the center of the heart. $B_1^{90^\circ}$ is approximately 1/16 G.

*Surface coil $B_1$ fields.* The field plots for surface coil simulations from 1.5 to 9.5 T are shown in Fig. 3. The power was adjusted in each simulation to obtain a 90° proton flip at the center of the heart. Note the increase in power requirement and $B_1$ field compression and distortion as the $B_0$ field increases. The asymmetry arises from taking the circularly polarized component of the RF field, shown explicitly in Eq. [6] and discussed in Ref. (*6*).

*Quantifying RF field distortion.* The field distortion observed from 1.5 to 4 T agrees qualitatively with the results of $B_1$ field mapping experiments on normal volunteers (*20*). Since full-body MRI machines do not currently exist beyond 4 T, the 6 and 9.5 T simulation data serve as a guide as to what one might expect at these fields. The static field dependence of the $B_1$ distortion motivated a method for quantifying distortion. We define the local fractional distortion, $l(x, y)$, as

$$l(x, y) = \frac{B_1^{\text{loaded}}(B_0) - B_1^{\text{unloaded}}(B_0)}{B_1^{90^\circ}}, \qquad [9]$$

where $B_1^{\text{unloaded}}(B_0)$ is the $B_1$ field, as defined in Eq. [6], for the unloaded coil at Larmor frequency $\gamma B_0$, and $B_1^{\text{loaded}}(B_0)$ is the $B_1$ field for the loaded coil at the same frequency. The loaded and unloaded fields have been normalized to the $B_1$ field at the center of the heart, $B_1^{90^\circ}$.

We define the absolute integrated distortion, $L$, as

$$L = \frac{\iint |l(x, y)|\,dA}{100A}, \qquad [10]$$

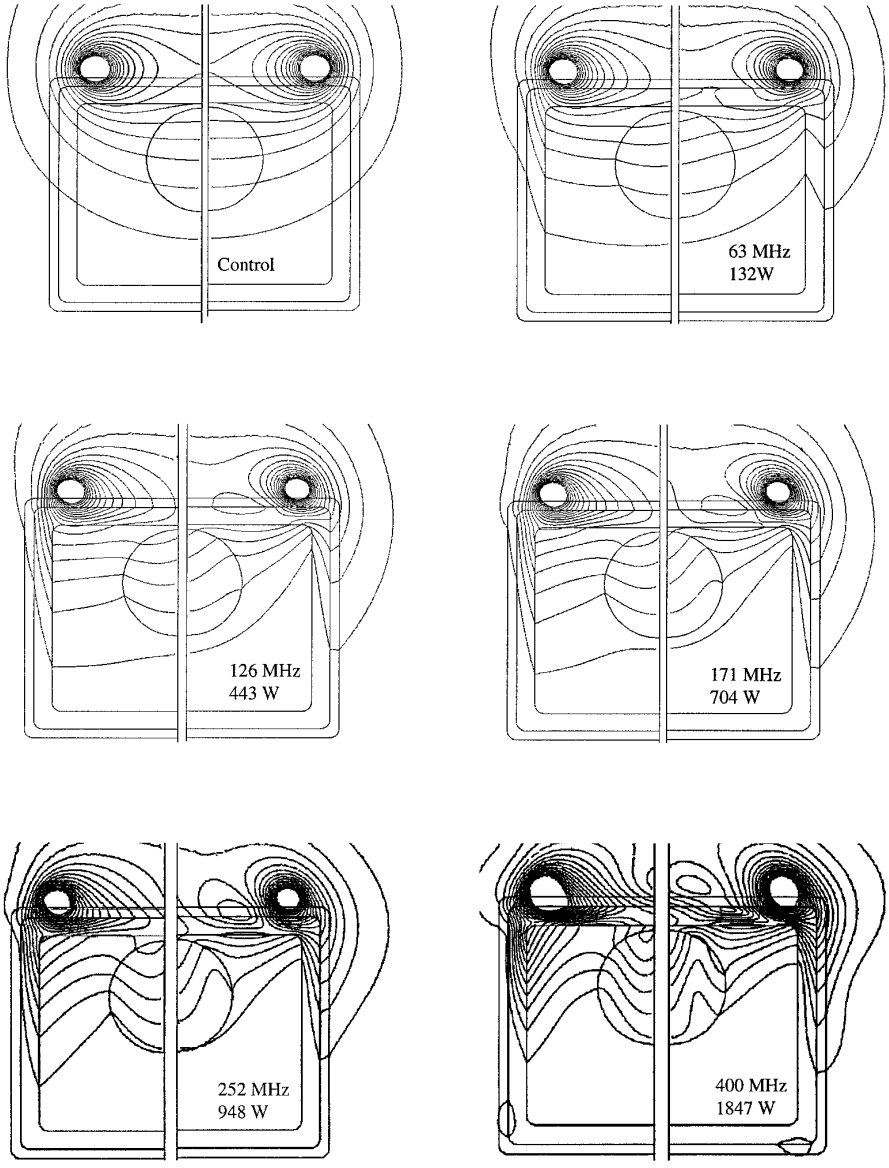


**FIG. 3.** Contour map of surface coil's RF field distribution in the chest for 1.5, 3.0, 4.0, 6.0, and 9.5 T. RF frequencies (proton Larmor frequencies) and associated required RF powers are shown. Required RF powers, $P_{90°}$, are for a 90° proton flip in the center of the heart with a 1 ms square pulse. Contours represent proton flip angles from 30° (furthest contour into the body) to 540° in 30° increments. The control simulation shows the RF field at 1.5 T for an unloaded surface coil (i.e., all body electrical parameters set to values in air). The simulation model chest layer thicknesses, a 1 cm thick fat layer and a 2 cm muscle layer, were chosen so that the model results bracketed experimental results on our normal volunteer at 1.5 T (*20*).

where the integral is done over the various body regions in the right half-plane of the simulation body model, and $A$ is the area of the given body region. For example, $L_{\text{heart}}$ is the integral of $|l(x, y)|$ over the heart in the right half-plane, normalized to the area of the heart in the right half-plane divided by 100. The factor of 100 is simply for scaling purposes. In general, $L$ is the measure of distortion of the RF field over a given region. The effects of field on $L$ for the various regions of the body are presented in Fig. 4. The distortion increases with static field.

*Estimating required power range for surface coil.* One of the goals of the simulation studies was to construct upper and lower bounds for RF power requirements as a function of static field. This would help define the range of RF power requirements for cardiac MRI studies on humans. To cover this range, a solid model was created in addition to the four-layer model (air-filled lungs) to bracket the potential experimental conditions. To create this solid model, the lung space was filled with blood. We refer to this solid model as the two-layer model since the heart, lung space, and chest

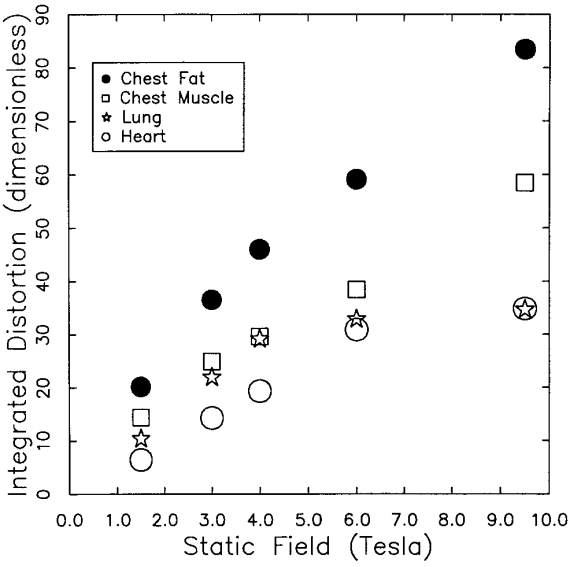


**FIG. 4.** Measure of distortion of RF field, in various body parts, as a function of static field.

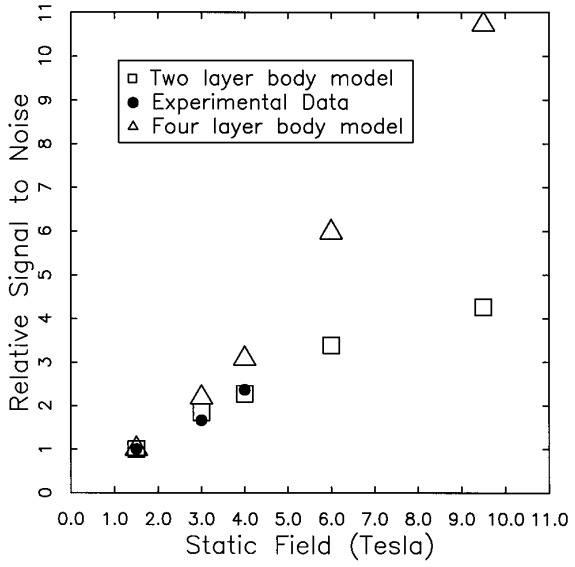


**FIG. 6.** Static field dependence of surface coil intrinsic signal-to-noise ratio (ISNR) for the two-layer and four-layer body models, and static field dependence of the experimental ISNR.

muscle are all muscle and blood. Blood and muscle are approximately the same material in terms of dielectric constant and conductivity. Hence, the two-layer model is a layer of fat surrounding a can full of muscle.

Figure 5 shows the simulation RF power results of the two-layer model (blood-filled lungs) and four-layer model (air-filled lungs). The chest layer thicknesses were chosen so that the models bracketed the experimental results at 1.5 T (*20*). Figure 5 also includes the measured powers from experimental data collected in this lab up to 4 T (*20*). These 3 and 4 T experimental points fall within the predicted range, suggesting that the model qualitatively represents the frequency dependency up to 4 T and may provide reliable estimates for higher fields.

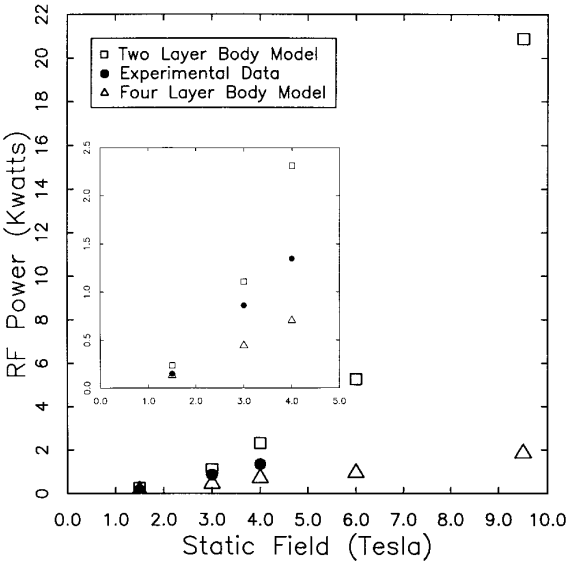


**FIG. 5.** Static field dependence of surface coil RF power deposition for the two-layer (blood-filled lung) and four-layer (air-filled lung) body models, and static field dependence of the experimental power requirements. Inset shows enlargement of 1.5, 3, and 4 T data.

*Intrinsic signal-to-noise ratio.* From the simulations, the relative ISNR was computed from the power required to produce a 1 ms 90° proton flip at the center of the heart from the following relation (*21*):

$$\text{ISNR} \sim B_0^2/\sqrt{P_{90^\circ}}. \qquad [11]$$

We define the relative ISNR of the receiver coil as $(\text{ISNR})_{\text{rel}} = (\text{ISNR})_{B_0}/(\text{ISNR})_{1.5\,\text{T}}$, where $(\text{ISNR})_{1.5\,\text{T}}$ is the ISNR at 1.5 T, and $(\text{ISNR})_{B_0}$ is the ISNR at static field $B_0$. Figure 6 shows the ISNR for four-layer and two-layer body models up to 9.5 T. The experimental ISNR data as a function of field in the heart from previous work (*20*) are also shown. Good correlation is found between the experimental data and simulation up to 4 T.

*RF power requirement as a function of body size.* We use the model to estimate the power variation as a function of body size at 1.5 and 4 T. Simulations were performed on four-layer models of varying fat and muscle thicknesses. Figure 7 illustrates the results where $P_{90^\circ}$ is plotted versus total chest wall thickness. The fat and muscle compositions of the four total thicknesses are as follows: 1.5 cm total thickness implies 0.5 cm fat thickness and 1.0 cm muscle thickness; 3.0 cm total thickness implies 1.0 cm fat thickness

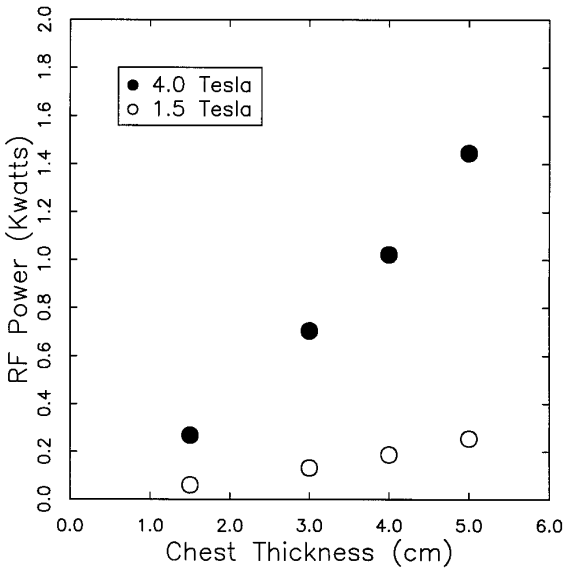


**FIG. 7.** RF power required for surface coil to produce a 1 ms 90° proton flip in the center of the heart, in the four-layer body model, as a function of chest wall thickness, at 1.5 and 4 T. Chest wall thickness is the sum of the chest muscle and chest fat thicknesses.

and 2.0 cm muscle thickness; 4.0 cm total thickness implies 1.5 cm fat thickness and 2.5 cm muscle thickness, which are NIH Visible Human Dimensions and 5.0 cm total thickness implies 2.0 cm fat thickness and 3.0 cm muscle thickness. Note the large absolute power levels required for the thicker chest walls at 4 T. Further, independent of chest wall thickness, the required power increased by a factor of $5.1 \pm 0.7$ in the step from 1.5 to 4.0 T. Hence an approximate factor of 5 serves as our lower limit for the expected power increase in stepping from 1.5 to 4 T.

*Body coil $B_1$ fields.* In cardiac MRI, homogeneous $B_1$ field excitation is desirable for numerous applications. Body coil excitation is one method for creating such a $B_1$ field. For the body coil RF field simulations, the four-layer model was used with a fat thickness of 1.5 cm and muscle thickness of 2.5 cm. Figure 8 shows the RF field intensity map of the loaded body coil at 1.5, 3.0, 4, and 6.8 T along with RF frequency and $P_{90°}$. For comparison, the RF field of the unloaded body coil at 1.5 T is shown. As with the surface coil, the RF field inhomogeneity increases as the static field, $B_0$, increases, and this can lead to image amplitude artifacts.

*Estimating required power range for body coil.* As with the surface coil simulations, we construct a theoretical range for expected experimental power requirements. To construct this power range, we performed a second set of simulations with the only change being that the lung space was filled with blood. Hence, we again have a solid model for determining the upper limit of the expected power range. Figure 9 shows the body coil simulation results for required power. In contrast to the surface coil experiments, we did not have access to experimental results to test our predictions. Rather, the simulation results should be interpreted as a guide to the power requirements and RF field distortions that should be taken into account in the design of high-field body coils. Beyond 6 T, the computed $P_{90°}$ values are not as straightforward to interpret. Above 6 T, the field distortion gets much more pronounced as standing wave modes of higher order become even more significant. At 6.8 T (285 MHz), this results in RF field amplification at the center of the heart and thus a lowered $P_{90°}$. This explains the dip in power for the last data point in Fig. 9. In contrast, at 300 MHz the simulation result is close to a node at the center of the heart. The resulting $P_{90°}$ is roughly 7000 times larger than the $P_{90°}$ for the only slightly lower frequency of 285 MHz. Hence, the redistribution of the $B_1$ field at this frequency has resulted in a factor of 80 decrease in SNR at the center of the heart. We intentionally do not give more precise values because the fields are so small at the center of the heart that the precision of the calculation is approached. Figure 10 shows the 300 MHz field data for the two-layer body model. Each brighter change in shade in the intensity map represents a 90° increase in the band of flip angles. The darkest shade represents flip angles from 0 to 90°. The value at the center of the heart is 15°. This ''threshold'' in radical field distributions is likely due to the approach of several dielectric resonances in this model in the region of 300 MHz.

*Comparing surface coil and body coil excitation.* We compare the total power and the peak local power depositions for the surface coil and body coil. For the comparison, we compute $P_{90°}$ for both coils on the same body model (four-layer model with approximate NIH Visible Human dimensions: chest fat thickness of 1.5 cm and chest muscle thickness of 2.5 cm). On this identical body model, the body coil required 847 W while the surface coil required 1022 W to achieve a 1 ms 90° proton flip at the center of the heart at 4 T. The greater surface coil power can be explained by noting that the body loads the surface coil more than the body coil. Alternatively, the effective filling factor for the surface coil is greater than that of the body coil.

The largest local power deposition for the surface coil occurs in the muscle layer just below the coil. Figure 11 shows the contours of local power deposition that corresponds to the above 1022 W total surface coil power deposition at 4 T. The local power maximum, 0.65 W/cm$^3$, occurs just below the interface between muscle and fat. The electric field, $\mathbf{E}$, at this point is $1.2 \times 10^3$ V/m. We note that the local power maximum does not occur at the top of the fat layer just below the coil, although this tissue is closer to the coil. Furthermore, $\mathbf{E}$ at this point is $2.0 \times 10^3$ V/m. Hence, the maximum dissipation point is not the same as the point of maximum electric field. This occurs because the conductivity, $\sigma$, of the muscle is approximately four times as great as the conductivity of fat, and the dissipation goes as $\sigma \mathbf{E}^2$.

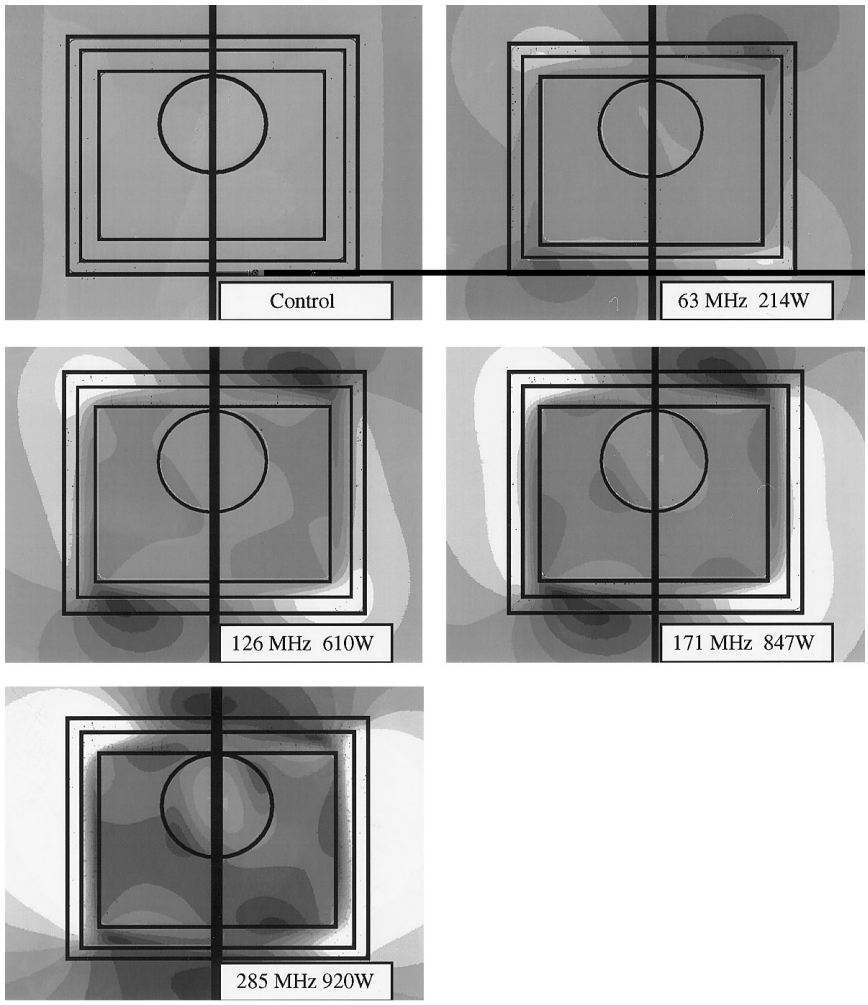


**FIG. 8.** Intensity map of body coil's RF field distribution in the chest for 1.5, 3.0, 4.0, and 6.8 T. RF frequencies (proton Larmor frequencies) and associated required RF powers are shown. Required RF powers, $P_{90°}$, are for a 90° proton flip in the center of the heart with a 1 ms square pulse. Regions are separated in field strength by 15° in proton flip angle. The control simulation shows the RF field at 1.5 T for an unloaded body coil (i.e., all body electrical parameters set to values in air). In comparison to the surface coil RF field simulations in Fig. 3, a larger body model, NIH Visible Human dimensions, was used here to simulate a more clinically relevant subject: fat layer 1.5 cm thick and muscle layer 2.5 cm thick.

Finally we note that the above total body coil power of 847 W produced a local power maximum of 0.10 W/cm$^3$. The local maximum for the surface coil, however, is 0.65 W/cm$^3$. Hence for producing the same RF field at the center of the heart with a body coil, the local power maximum is a factor of 6.5 less.

## DISCUSSION

*Justifying the model.* First and foremost, one could claim that the model is too oversimplified to produce physically meaningful results. We argue against this claim on the basis of the model's ability to produce results consistent with experiment. In particular, at 3 and 4 T, the highest fields for which experimental RF field mapping data in the chest are available, the simulations qualitatively reproduce the experimental behavior of the RF field in the heart and chest. Furthermore, the 3 and 4 T experimental signal-to-noise ratios at the center of the heart and the experimental power requirements fall within the ranges predicted by the model. Indeed, the modeling strategy was based on the idea of bracketing the range of expected results with two simplified models as opposed to developing a single complex model. Since the model does achieve the goal of bracketing experimental results and qualitatively reproduces the experimental RF magnetic field distortion in the chest, it is physically meaningful.

As for RF field simulations for imaging beyond 4 T, dielectric focusing effects could certainly become more significant. Ideally, nonsymmetric 3D simulations would be performed. However, large computational resources and large computational times are required for such simulations. For our axially symmetric simulation results at 4 T and

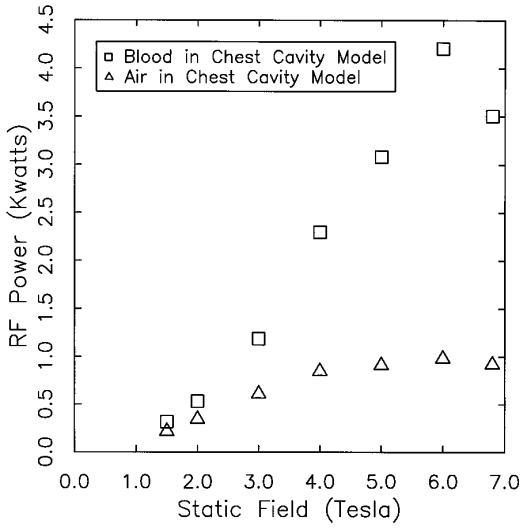


**FIG. 9.** Static field dependence of body coil power deposition in the two-layer (blood-filled lung) and four-layer (air-filled lung) body models.

below, however, the dielectric focusing effects appear to be small as borne out by the aforementioned consistency of simulations with experiment. Clearly, any model that extends beyond currently available experiments (beyond 4 T in the present case) becomes less certain in the new regime. The purpose of the model in the extended regime, however, is to present possible physical phenomena that should be considered at the higher fields. Nowhere is this more poignant than in the node at the center of the heart that occurred for a surface coil at 300 MHz. Such a node might not appear at the center of real person's heart, but such strong attenuation might appear off center—especially since multiple wavelengths of the RF field fit across the chest at 300 MHz. Certainly, the increased distortion at high static field is a parameter to consider in the proposed advancement of imaging beyond 4 T.

*Computational factors determining choice of model.* Earlier simulations (*12, 13*) used two-dimensional (and thus infinitely long) body models. These body models, however, do not capture the three-dimensional nature of the wave vectors and the resulting dispersion relation. This problem in the relation between length and time scales (wave vector and frequency) is exacerbated as the static magnetic field is increased. In particular, as the static field is increased to 4 T, the proton Larmor frequency reaches 170 MHz. At this frequency, the displacement current

$$\frac{1}{c}\frac{\partial \epsilon \mathbf{E}}{\partial t} \qquad [12]$$

becomes comparable to the eddy current in the body,

$$\frac{4\pi\sigma\mathbf{E}}{c}. \qquad [13]$$

Furthermore, the corresponding RF wavelength in heart tissue, 22 cm, becomes comparable to the size of the heart. Solving a full nonsymmetric three-dimensional model, however, requires large computation resources. As a compromise between these issues, we chose a symmetric, heterogeneous, three-dimensional model composed of spheres and finite size cylinders. In this way, we could generate three-dimensional solutions by solving Maxwell's equations in polar coordinates in a two-dimensional half-plane.

For body coil simulations, one would ideally like to employ a birdcage coil driven in quadrature (*6*). However, such a coil would break the axial symmetry of our model. Hence, from the point of view of simulating the body in an approximately uniform RF field, the compensated solenoid yields the computational advantage of being symmetric with respect to the body model. Therefore, one can still perform a three-dimensional axially symmetric calculation by solving Maxwell's equations in two-dimensional cylindrical coordinates.

*Interpretation of electrical parameters.* The power calculations depend strongly on the values of the electrical parameters such as dielectric constant and conductivity. We briefly expand on the physical source of the RF conductivity and RF loss. Starting with the equation for the curl of the magnetic field (*22*), the frequency-domain equation for the curl can be written as

$$\nabla \times \mathbf{B} = \frac{4\pi}{c}\mathbf{J}_{\text{coils}} + \frac{4\pi}{c}\sigma_{\text{charges}}\mathbf{E} + \frac{i\omega\epsilon_c}{c}\mathbf{E} \qquad [14]$$

$$= \frac{4\pi}{c}\mathbf{J}_{\text{coils}} + \frac{4\pi}{c}\sigma\mathbf{E} + \frac{i\omega\epsilon}{c}\mathbf{E}, \qquad [15]$$

where $\epsilon_c$ is the complex dielectric tensor which is taken as the complex scalar $\epsilon_c = \epsilon - i\epsilon''$. $\epsilon$ and $\epsilon''$ are the real and imaginary parts, respectively, of the dielectric tensor.

The net conductivity associated with the RF losses in the body is given by

$$\sigma = \sigma_{\text{charges}} + \frac{\omega\epsilon''}{4\pi}. \qquad [16]$$

The term $\sigma_{\text{charges}}$ is due to losses associated with the translational motion of charge carriers, and $\epsilon''$ is associated with the dielectric loss. For example, dielectric loss can occur when the permanent electric dipoles of water try to align with the electric field. In particular, water molecules form hydration spheres around neighboring ions, and the resulting complexes have hindered rotational motion which causes dissipation (*18*). The behavior of the water and ion complexes is of special interest in our frequency range because the tissue electrical properties above 100 MHz are determined in large part by the water content of the tissue (*18*). Experimentally, $\epsilon$ and $\sigma$ are inferred from transmission line measurements. In

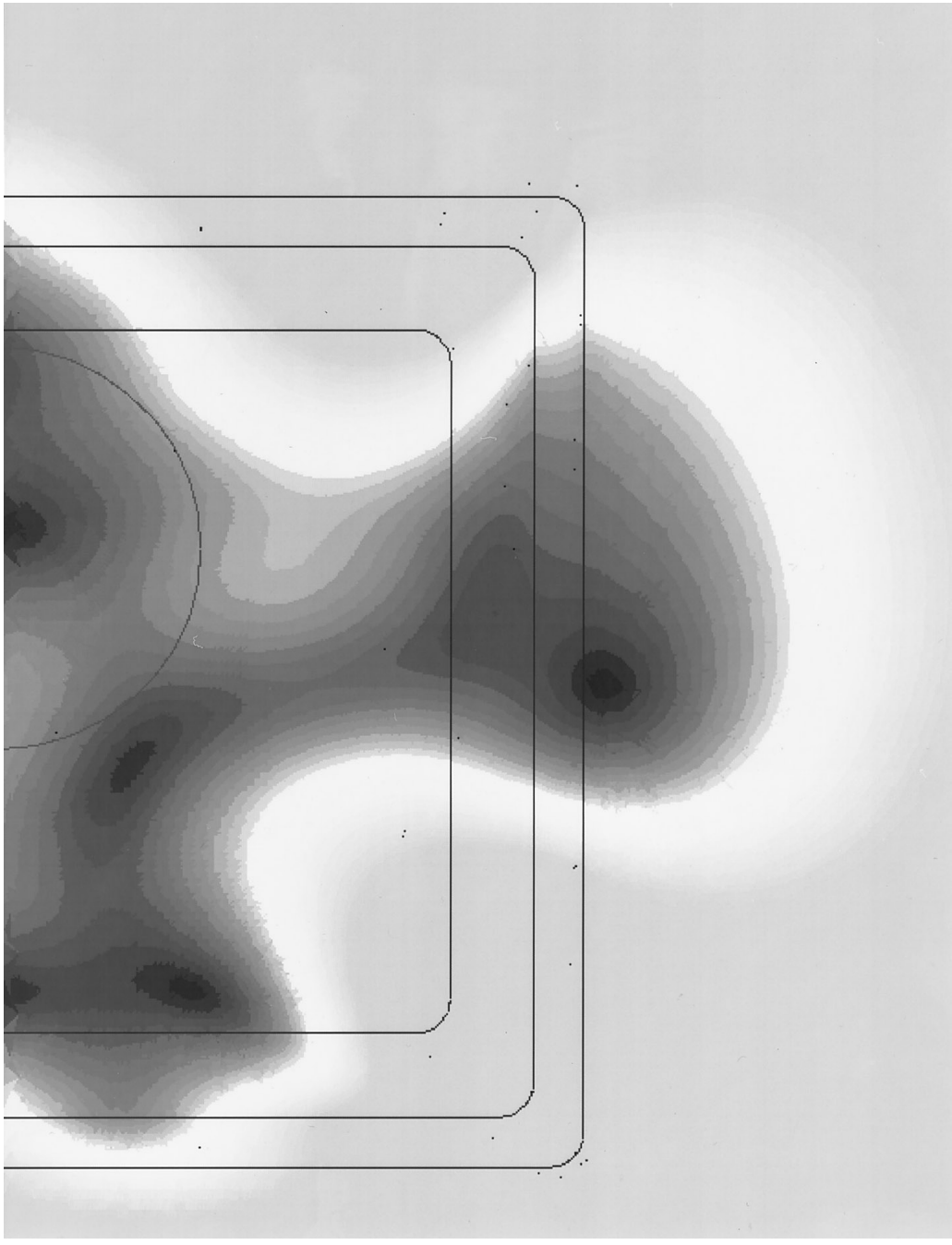

**FIG. 10.** Intensity map of body coil's RF field distribution, on the right side of the chest, at 300 MHz (approximately 7.1 T). The two-layer body model (blood-filled lung) with NIH Visible Human dimensions is used. Note approximate node at the center of the heart.

particular, they are determined from impedance measurements of *in vivo* tissues terminating transmission lines (*16*). These measurements yield values for $\sigma$ that represent the combined conductive and dielectric losses.

*Imaging with lower gamma nuclei.* The significant total and local powers deposited in large individuals at 4 T and above, as compared to 1.5 T, will curtail the rapidity and magnitude of RF excitation due to safety limits for overall and local power deposition. Imaging lower $\gamma$ nuclei at high fields has been suggested to avoid power deposition issues. A general relationship between $P_{90^\circ}$ and magnetic field can be derived which demonstrates that $P_{90^\circ}$ scales with field and not $\gamma$. This relation is derived below using the quasi-static approximation,

$$P_{90^\circ} = \alpha \omega_L^2 B_1^2 \qquad [17]$$

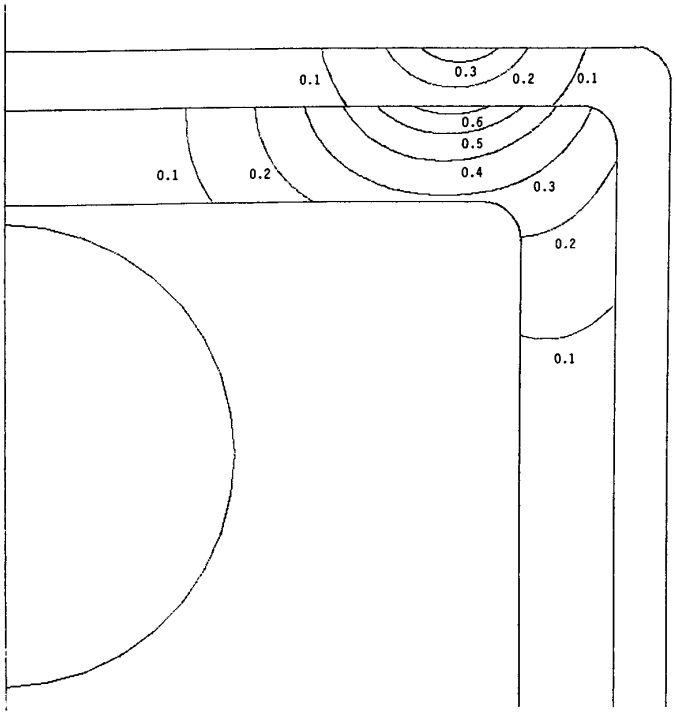


**FIG. 11.** Surface coil local power distribution in the chest at 4.0 T. Contours are in increments of 1 W/cm$^3$. The volume integral of this local power distribution over the chest yields a $P_{90°}$ of 1022 W. A four-layer body model (air-filled lungs) with NIH Visible Human dimensions is used. Fat thickness is 1.5 cm. Muscle thickness is 2.5 cm. Heart diameter is 12 cm.

$$\theta_{90°} = B_1 \gamma \tau \qquad [18]$$

$$P_{90°} = \alpha(\gamma B_0)^2 \frac{\theta_{90°}^2}{(\gamma\tau)^2} \qquad [19]$$

$$P_{90°} = \alpha \frac{(B_0\theta_{90°})^2}{\tau^2}, \qquad [20]$$

where $\alpha$ is a geometrical factor independent of field and nuclear species, and $\omega_L$ is the Larmor frequency. From Eq. [20], $P_{90°}$ scales with $B_0^2$ independent of $\gamma$. We note that the same flip angle and the same RF pulse duration are used for the different nuclides. Based on the squared increase in power deposition with frequency, and the fact that much of the $S/N$ per unit time with sodium-23 and other nuclides is obtained by rapid, high-angle, pulsing of these rapidly relaxing spins, there may be actual disadvantages of using low $\gamma$ nuclides at higher fields in terms of the specific absorption rate (SAR). However, it is clear that the lower $\gamma$ nuclides will have smaller dielectric terms distorting and compressing the $B_1$ field as demonstrated in these simulations for protons at a given magnetic field strength. Complex multinuclear spectroscopy experiments, however, would require further analysis. Finally, we note that RF coils are generally more efficient at lower frequencies due to reduced radiation, not considered in Eq. [20], which decreases the coil input power requirements for low $\gamma$ nuclides but does not decrease the SAR.

## IMPLICATIONS OF SIMULATIONS

In general, good correlations between experimental data and simulations were obtained up to 4 T. In extending the model to fields up to 9.5 T, the main implications of the model are the increased distortion and power deposition. One of the major causes of this distortion is the onset of resonant modes in the body. Such resonances become possible when the RF wavelength in tissue becomes comparable to the size of the tissue. For example, at 171 MHz, the heart is approximately a half-wavelength. With regard to power deposition, the quasi-static prediction of a $B_0^2$ increase in power fell between the two-layer and four-layer model results, but was closest to the two-layer model (blood-filled lung). In the four-layer model (air-filled lung) the lack of lossy material in the lung space allows for more resonant energy to be built up at the center of the heart, resulting in a more efficient delivery of $B_1$ to the heart at higher static fields than the quasi-static prediction. These power requirements implied a slightly less than linear increase in ISNR for the two-layer model and a greater than linear increase in ISNR for the four-layer model up to 9.5 T. The two-layer and four-layer models defined upper and lower limits for power and ISNR. The experimental results had a slightly less than linear ISNR dependence on field and a slightly greater than quadratic power dependence on field. Within experimental error, the combination of the two-layer and four-layer models did indeed bracket experimentally expected results. Hence the range of power, range of ISNR, and range of scaling with static field predicted by the model are consistent with the experimental results (*20*).

In extending the results beyond the regime of present-day MRI magnets, a large increase in distortion with field up to 9.5 T was observed in the body and surface coil simulations. For the body coil, the increase in field distortion due to the onset of higher modes strongly argues against homogeneous whole-body imaging beyond 6 T due to the dramatic inhomogeneity in the $B_1$ field. The $B_1$ distortion with surface coils will also influence the ability to use phased array designs since coil isolation will be difficult to achieve (*20*).

## ACKNOWLEDGMENTS

Thanks go to the members of the Laboratory of Cardiac Energetics and the In Vivo NMR Center for creating a stimulating environment. A special thank you goes to the system administrator, Chris Olaes.

## REFERENCES

1. D. I. Hoult and P. C. Lauterbur, *J. Magn. Reson.* **34,** 425 (1979).
2. P. A. Bottomley and E. R. Andrew, *Phys. Med. Biol.* **23,** 630 (1978).

3. P. A. Bottomley and W. A. Edelstein, *Med. Phys.* **8,** 510 (1981).
4. P. Mansfield and P. G. Morris, ''NMR Imaging in Biomedicine,'' p. 182, Academic Press, New York, 1982.
5. P. A. Bottomley, R. W. Redington, W. A. Edelstein, and J. F. Schenck, *Magn. Reson. Med.* **2,** 336 (1985).
6. G. H. Glover, C. C. Hayes, J. J. Pelc, W. A. Edelstein, O. M. Mueller, H. R. Hart, C. J. Hardy, M. O'Donnell, and W. D. Barber, *J. Magn. Reson.* **64,** 255 (1985).
7. M. D. Harpen, *Phys. Med. Biol.* **33,** 597 (1988).
8. M. D. Harpen, *Med. Phys.* **17,** 362 (1990).
9. J. R. Keltner, J. W. Carlson, M. S. Roos, S. T. S. Wong, T. L. Wong, and T. F. Budinger, *Magn. Reson. Med.* **22,** 467 (1991).
10. R. W. Brown, E. M. Haacke, M. A. Martens, J. L. Patrick, and F. R. Zypman, *J. Magn. Reson.* **80,** 225 (1988).
11. L. S. Petropoulos and E. M. Haacke, *J. Magn. Reson.* **91,** 466 (1991).
12. M. B. Smith, C. N. Ashtiani, Z. J. Cendes, G. D. Williams, and J. T. Martin, *Proc. Soc. Magn. Reson. Med.,* 995 (1989).
13. T. Denison, H. Wen, M. Smith, and R. Balaban, *Proc. Soc. Magn. Reson. Med.,* 967 (1995).
14. W. A. Edelstein, G. H. Glover, C. J. Hardy, and R. W. Redington, *Magn. Reson. Med.* **3,** 604 (1986).
15. D. I. Hoult, C. N. Chen, and V. J. Sank, *Magn. Reson. Med.* **3,** 730 (1986).
16. E. C. Burdette, F. L. Cain, and J. Seals, *IEEE Trans. Microwave Theory Tech.* **MTT-28,** 414 (1980).
17. E. C. Burdette, F. L. Cain, and J. Seals, ''Medical Applications of Microwave Imaging'' (L. E. Larsen and J. H. Hacobi, Eds.), p. 13, IEEE Press, New York, 1986.
18. R. Pethig and D. B. Kell, *Phys. Med. Biol.* **8,** 933 (1987).
19. M. W. Garrett, *J. Appl. Phys.* **38,** 2563 (1967).
20. H. Wen, R. Singerman, and R. S. Balaban, *Proc. Int. Soc. Magn. Reson. Med.* **1,** 254 (1996).
21. H. Wen, A. S. Chesnick, and R. S. Balaban, *Magn. Reson. Med.* **32,** 492 (1994).
22. J. D. Jackson, ''Classical Electrodynamics,'' Wiley, New York, 1975.
23. E. M. Purcell, ''Electricity and Magnetism,'' McGraw–Hill, New York, 1985.